A Four-Channel BiCMOS Transmitter for a Quantum Magnetometer Based on Nitrogen-Vacancy Centers in Diamond

Hadi Lotfi, *Graduate Student Member, IEEE*, Michal Kern, Qing Yang, Thomas Unden, Nico Striegler, Jochen Scharpf, Patrick Schalberger, Rainer Stöhr, Ilai Schwartz, Philipp Neumann, and Jens Anders, *Senior Member, IEEE*

Abstract— Quantum sensors based on solid-state defects, such as the nitrogen-vacancy (NV) center in diamond, offer very good room-temperature sensitivity, long-term stability, and the potential for calibration-free measurements. However, most quantum sensors still suffer from a bulky size and weight, low energy efficiency, and high costs, prohibiting their widespread use. Here, we present custom-designed chip-integrated microwave (MW) electronics for a miniaturized, low-cost, and highly scalable quantum magnetometer based on NV centers in diamond. The presented electronics include a quadrature phase-locked loop (QPLL) chip to generate the required local oscillator signal at around 7 GHz with a wide tuning range of 22% and a low phase noise (PN) of −122 dBc/Hz at 1-MHz offset from a 7-GHz carrier for broadband low-noise magnetometry. In addition, the magnetometer electronics comprise a 4-channel transmitter chip, which can provide currents up to 412 mA$_{pp}$ into a custom-designed inductor over a wide frequency range from 6.4 to 8 GHz. In combination with a custom-designed coil, manufactured on a glass substrate for optical transparency, which features a large active area of ($\pi \times 180 \times 180 \ \mu m^2$), this current is sufficient to produce strong MW magnetic fields up to $B_1 = (1/2) \cdot B_{ac} = 170 \ \mu T$, enabling pulsed optically detected magnetic resonance (ODMR) experiments. In proof-of-concept ODMR experiments, the presented chip-based spin control system produces fast Rabi oscillations of 5.49 MHz. The measured dc and ac magnetic field limits of detection (LOD) of the presented magnetometer are 32 nT/Hz$^{1/2}$ and 300 pT/Hz$^{1/2}$, respectively.

Hadi Lotfi, Michal Kern, and Qing Yang are with the Institute of Smart Sensors, University of Stuttgart, 70569 Stuttgart, Germany (e-mail: hadi.lotfi@iis.uni-stuttgart.de).

Thomas Unden, Nico Striegler, Jochen Scharpf, Ilai Schwartz, and Philipp Neumann are with NVision Imaging Technologies GmbH, 89081 Ulm, Germany.

Patrick Schalberger is with the Institute for Large Area Microelectronics, University of Stuttgart, 70569 Stuttgart, Germany.

Rainer Stöhr is with the 3. Physics Institute, University of Stuttgart, 70569 Stuttgart, Germany.

Jens Anders is with the Institute of Smart Sensors, University of Stuttgart, 70569 Stuttgart, Germany, also with the Institute for Microelectronics Stuttgart, 70569 Stuttgart, Germany, and also with the Center for Integrated Quantum Science and Technology (IQST), 70569 Stuttgart, Germany.

Index Terms— Nitrogen-vacancy (NV) centers, optically detected magnetic resonance (ODMR), power amplifier (PA), quadrature phase-locked loop (QPLL), quantum sensor, radio frequency transmitter (RF TX), SiGe BiCMOS.

I. INTRODUCTION

SECOND-GENERATION quantum sensors harness the potential of manipulating individual quantum bits (qubits) to measure various physical quantities with unparalleled precision. Here, room-temperature quantum sensors mostly use either gases or defects in solids as sensing media. Due to the weaker interaction of the individual atoms, atomic-gas qubits usually provide longer coherence times and, therefore, higher sensitivities but are typically harder to integrate and miniaturize. In contrast, defects in solids provide a lower sensitivity while offering the potential for small, scalable, low-cost quantum sensors with a performance that can still outperform most classical sensors. To name just a few examples, nitrogen-vacancy (NV) centers in diamond have been used to construct ultra-stable time references [1], measure the magnetic field associated with neuromuscular signals [2], detect magnetic nanoparticles in biomedical applications with a very high resolution [3], image at the atomic scale [4], and perform nanometer-scale thermometry inside living cells [5]. Moreover, thanks to the optical hyperpolarization and optical readout of the NV center in optically detected magnetic resonance (ODMR) experiments, NV center sensors can be used to perform nuclear magnetic resonance (NMR) experiments on the nanoscale down to single molecules [6]. Conventional diamond magnetometers [7], [8], [9] use costly and bulky high-end signal generators together with commercial power amplifiers (PAs), driving simple wire structures to produce the required microwave (MW) magnetic fields, B_1, which are needed to control the spin qubits. These architectures lead to poor energy efficiency, frequently requiring tens to hundreds of watts of output power to produce the necessary MW fields of typically a few gauss to a few tens of gauss. To address this issue, recently, chip-integrated solutions that produce the required MW magnetic fields using on-chip frequency synthesizers and on-chip current drivers [10] or arrays of metal stripes in an on-chip phase-locked loop (PLL) [11], a voltage-controlled oscillator (VCO) integrated with a filtering antenna [12], or an array of injection-locked VCOs [13] have been
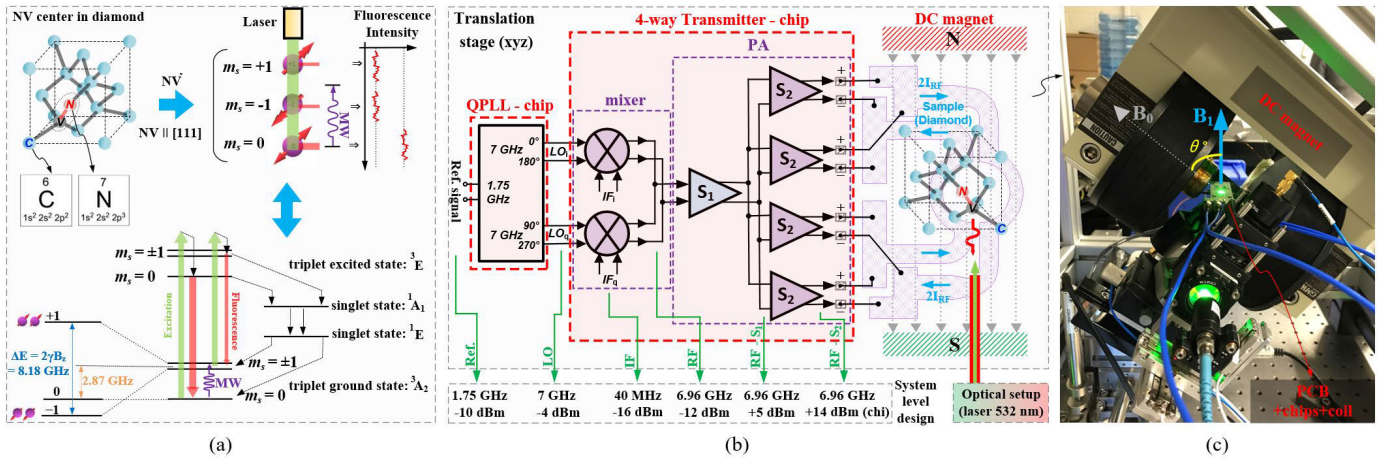
Fig. 1. ODMR magnetometry. (a) Simplified energy-level diagram of the NV center in a diamond for a situation where the Zeeman splitting is greater than the zero-field split. (b) Architecture of the presented quantum magnetometer. (c) ODMR measurement setup including the electromagnet, the presented MW ASICs, the custom-designed coil, and the optical setup.

proposed. However, the VCO-based approach suffers from limited coil sizes, limited coil currents, and difficulties in producing pulsed excitations with arbitrary phase control with high timing resolutions [14]. More specifically, in the VCO-based approach, varying the coil size leads to a direct tradeoff between the oscillator's phase noise (PN) and tuning range, while the maximum coil current is limited by the oscillator's supply voltage and/or the large voltage swing across the active devices inside the VCO. In contrast, the approach of using on-chip inductors (spiral inductors and/or stripe arrays) that are not embedded into a VCO allows for arbitrary phase and frequency modulation but comes with a cost tradeoff if large active volumes are needed. To address these issues, in this article, we present a quantum magnetometer with chip-integrated electronics that uses a 4-channel BiCMOS transmitter for enhanced driving capabilities in combination with an off-chip, custom-designed coil structure on a glass substrate to provide a large MW magnetic field B_1 over a large 3-D volume without compromises in the PN and/or the arbitrary phase control of the system.

This article, which is an extended version of [15], is organized as follows. Section II provides a brief summary of the ODMR method to facilitate understanding the tradeoffs in the design of ASICs for this application. Sections III–V then describe the architecture of the presented quantum magnetometer and the circuit implementations of the chip-integrated transmit electronics and the custom-designed off-chip coil. The electrical characterization and the ODMR magnetometry measurements obtained with the presented system are discussed in Section VI, before we conclude this article with a summary and a brief outlook on future work in Section VII.

II. ODMR ON NV CENTERS IN DIAMOND

In this section, we will discuss the physical operating principle of NV magnetometers. The discussion will be used to introduce the requirements of the MW electronics presented in this article and otherwise kept to a minimum. The interested reader can find more details on the physics of the NV center in [16]. The NV center contains two unpaired electrons

forming a spin triplet, resulting in the energy-level diagram shown in Fig. 1(a). The spin triplet consists of $|m_s = 0\rangle$ and $|m_s = \pm1\rangle$ spin states, separated by a zero-field splitting of ~2.87 GHz. The NV center can be excited from its ground state ($^3A_2$) to the excited state (^3E) using a 532-nm green laser light. From the excited (^3E) state, the electrons decay either by emitting a red fluorescence photon or through the meta-stable singlet states ($^1A_1$ and ^1E) after a non-radiative inter-system crossing (ISC). There are two important characteristics of the ISC relaxation pathway: 1) the probability of the ISC relaxation pathway is higher for $|m_s = \pm1\rangle$ states and 2) the system will preferentially relax back to $|m_s = 0\rangle$ state. Therefore, applying the green 532-nm laser for a sufficient time initializes the system into $|m_s = 0\rangle$ state. In addition, by irradiating the system with an MW field, B_1, at a frequency of $f_{MW} = 2.87$ GHz $\pm (\gamma/2\pi)B_0$, where $\gamma \approx 2\pi \cdot 28$ GHz/T is the so-called gyromagnetic ratio, and B_0 is an external magnetic field, the spin states can be excited from $|m_s = 0\rangle$ into $|m_s = \pm1\rangle$ states. This spin manipulation results in a change in the red fluorescence signal, allowing for optical detection of the spin transitions. The technique is called ODMR. Typical fluorescence signal contrasts are between 0.1% and 5%, depending on the used sample and other experimental conditions, but higher values can be reached under specific conditions [17]. A change in the magnetic field B_0 leads to a splitting of the resonance lines associated with $|m_s = \pm1\rangle$ states by $\Delta f = 2(\gamma/2\pi)B_0$, which allows for precise extraction of the value of B_0 from the measured Δf. The measurement of dc magnetic fields is still frequently carried out using continuous-wave (CW) MW excitation [11]. CW measurements can be performed both by sweeping the static magnetic field B_0 or by sweeping the excitation frequency f_{MW} at a fixed B_0 field. Here, the frequency-sweep mode is preferable since it allows for operation with a compact and miniaturizable permanent magnet, but it requires a sufficient sweep range of the MW electronics. In contrast, the measurement of highly localized ac magnetic fields, such as those produced by nuclear spins in nano- and micro-scale NMR spectroscopy, the target application of the

system presented in this article, requires advanced pulsed MW excitation schemes [18]. Pulsed experiments are mostly carried out at a fixed B_0 field but require larger B_1 fields than CW experiments, imposing more stringent requirements on the coil driver. Moreover, pulsed experiments require a better homogeneity of the B_1 field to ensure constant flip angles over the NV center ensemble and, thereby, maximum signal intensity. Here, the required size of the active volume largely depends on the target application. While for many applications, such as single-cell NMR, the required active volume is limited by the laser spot size, which for the presented system is approximately $(20 \ \mu m)^2$, much larger active volumes can be required if the laser spot is scanned over a larger area, e.g., to measure NMR on cell arrays. Similarly, large active volumes of the B_1 field are required if a parallel readout for throughput enhancement is required [19].

III. SYSTEM ARCHITECTURE

As discussed in Section II, an ODMR experiment with NV centers in diamond requires an optical setup that excites and detects the NV center's optical transitions as well as a setup to generate the MW magnetic field B_1 that allows for manipulation of the NV center's spin states.

The architecture of the presented NV-center-based magnetometer is shown in Fig. 1(b). According to Fig. 1(b), the optical setup uses conventional optical components, while the entire MW generation part is integrated into two separate ASICs, one quadrature PLL (QPLL) chip that synthesizes the required MW signal around 7 GHz and one 4-channel MW driver chip that drives the off-chip, custom-designed coil that produces the B_1 field which interacts with the spin of the NV center. The architecture of the transmitter electronics is shown in Fig. 1(b). According to Fig. 1(b), the quadrature outputs of the PLL chip drive the quadrature modulator on the 4-channel transmitter chip. Here, a quadrature modulator is used because, in combination with a linear driver, it provides the possibility of arbitrary phase and amplitude modulation of the MW B_1 field, as it is required by most modern ODMR pulse sequences.

The target application of the presented system is nano- and microscale NMR on biological cells [6], which introduces a unique set of requirements compared with conventional low-field magnetometry. An elevated B_0 field is required to provide sufficient spectral resolution and spin polarization of the nuclei of interest (primarily hydrogen and carbon). The elevated B_0 field helps differentiate between different nuclear spins inside a certain molecule via their chemical shift [20], which increases linearly with B_0. Hence, in contrast to previous chip-integrated spin control platforms, the presented setup shown in Fig. 1(b) and (c) also contains an electromagnet to generate this static magnetic field B_0. Here, we have chosen B_0 of ≈ 150 mT, which corresponds to NV center frequencies around 7 GHz and nuclear Larmor frequencies of 6.4 and 1.6 MHz for hydrogen and carbon nuclei, respectively. While even higher fields would be more beneficial for enhancing the spectral resolution of the ODMR signal [21], a B_0 field of 150 mT is still easily produced over a large volume with a conventional, relatively compact electromagnet, and the requirements on the field orientation and MW electronics are

still relaxed compared with even higher B_0 fields [21]. The target micro- and nano-scale NMR measurements make use of relatively long sequences of short MW pulses with varying phases (e.g., the widely used Qdyne protocol [18]). This places relatively strict requirements on the PN and I/Q mismatch of the MW system, as phase imbalances/phase errors between the pulses will result in the deterioration of the signal of interest. Unlike in a transmitter for a certain wireless standard, in the presented experimental prototype for NV-based NMR measurements, there is no fixed specification for the B_1 strength, the PN, and the phase imbalance performance. In contrast, the goal of this work is to establish an experimental platform that explores the maximally achievable performance in this regard to support as many as possible current and future pulse sequences as possible.

In addition, for many applications, the TX output power should be sufficient to generate effective Rabi frequencies close to the Larmor frequencies of the nuclei of interest. The homogeneity of the generated B_1 field across the active area should be maximal ($\geq 90\%$) to maintain consistent flip angles across the sample. Here, a homogeneity of 90% can be corrected by shaped pulsed that uses a varying phase and/or amplitude.

IV. TX FRONTENDS FOR SPIN MANIPULATION

In this section, we present a design approach for the TX frontend consisting of the coil driver, an appropriate impedance matching network, and the inductive structure that produces the B_1 field, which relates the ODMR specification, i.e., the required B_1 field and the active area to the required electrical attributes of the coil driver and the matching network. In this discussion, we will also highlight the main differences between the design of matching networks for conventional PAs and those required in TX frontends for efficient spin manipulation.

In conventional PAs, the primary objective of the output matching network (OMN) is to ensure maximum power transfer from the active device to a resistive load. In contrast, when dealing with a linear, class-A frontend for efficient spin control, the OMN should maximize the current flowing in the mostly inductive load to maximize the resulting MW magnetic field B_1. More specifically, the load inductor, apart from parasitic losses in its coil resistance, in principle, requires no active power to produce the B_1 field.

To design an optimum MW frontend for spin control in NV magnetometers, the following factors should be considered: 1) the coil should provide a high Q-factor, Q_c, to minimize parasitic losses while providing the largest possible active area to maximize magnetometer performance and 2) the OMN between the coil and the coil driver should transfer the coil impedance with its low real value, R_c, and its large positive reactance to the optimum load impedance of the PA ($Z_{L,\text{opt}} = R_{L,\text{opt}} + jX_{L,\text{opt}}$). Here, $Z_{L,\text{opt}}$ is the optimum load impedance at which the active device delivers the maximum output power, which can be determined through a large-signal load-pull simulation [22], [23].

To address the first point, the coil should be designed using EM simulations considering both the skin and the proximity
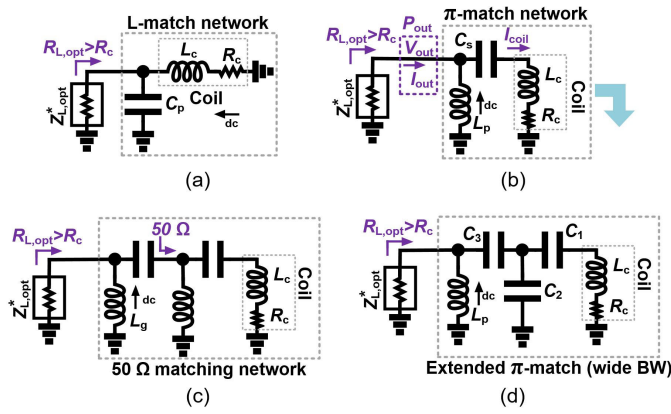
Fig. 2. Different matching networks for maximizing the output power of the active device and the current swing in the coil simultaneously. (a) Parallel *LC*-resonator. (b) Series *LC*-resonator (SLC). (c) Conventional matching structure (50 Ω). (d) Extended series *LC*-resonator for wideband designs (SLC-WB).

effect, which largely determine the effective ac resistance at the target operating frequency around 7 GHz. The choice of a suitable OMN depends on the parameters of the coil at hand and $Z_{L,\text{opt}}$. For coils with a high-quality factor, we typically have $R_{L,\text{opt}} > R_c$, and, in principle, both an L-matching network (parallel LC) and a π-matching network (series LC), as shown in Fig. 2(a) and (b), can be used. In both the designs, the existing inductors can be reused to provide the dc biasing path for the active cell of the coil driver. The coil producing the B_1 field can be implemented both on-chip or off-chip. The former option offers the advantage of removed bondwire inductances but comes at the cost of an increased chip area. The latter implementation increases design flexibility, allowing one to try out different coil designs after chip manufacturing but suffers from constraints imposed by the bondwire inductance. Here, depending on the topology, in principle, the bondwire inductance can be included in the matching network. Assuming a lossless matching network, for both the L- and the π-network, the coil current, $I_{\text{coil}}(\omega)$, can be related to the actual output power of the PA, P_{out}, according to

$$I_{\text{coil-rms}}(\omega) = \sqrt{\frac{P_{\text{out}}(\omega)}{R_c}}. \tag{1}$$

Interestingly, the assumption of a lossless OMN removes the dependence of the coil current on the current gain of the matching network and, under this assumption, the coil current is maximized by maximizing the output power P_{out} by matching the coil impedance to the optimum output impedance of the PA. To demonstrate the advantages of the proposed π-matching network, we compared it to a conventional 50-Ω matching presented as used in [24] and [25]. The corresponding results are shown in Fig. 3(a). According to Fig. 3(a), the 50-Ω match results in a somewhat lower absolute coil current. Moreover, a conventional 50-Ω-matching network, as shown in Fig. 2(c), would require an additional, typically large-valued series or parallel inductor, greatly increasing the die area of the 4-channel TX chip. Finally, the relatively large required inductors, which would be in the range of several nH

for the presented design, can have self-resonance frequencies (SRFs), which are not compatible with operation at the desired operating frequency around 7 GHz.

To relate the required output power P_{out} to the specifications of the quantum sensor, we need to relate the coil current to the MW magnetic field B_1 produced by the coil structure. Since at the target operating frequency of around 7 GHz and the required large coil size of $\gg 100\ \mu$m, it is hard to use multi-turn coils, we can approximate the resulting B_1 field using the closed-form expression for the magnetic field of a loop coil along its axis, taking into account an additional factor of $1/2$ due to the fact that B_1 is only one of the two circularly polarized components of the linearly polarized field along the coil axis, resulting in

$$B_1 = \frac{\mu_0 I_{\text{coil}}}{4} \cdot \frac{r^2}{\sqrt{(r^2 + z^2)^3}} \tag{2}$$

where μ_0 is the free-space permeability, and r and z are the radius of the coil and the distance of NV center from the coil surface, respectively. Here, only one of the two circularly polarized components of the linearly polarized MW magnetic field B_{ac} resonantly interacts with the spin ensemble. This phenomenon is known in quantum mechanics as the rotating wave approximation. A good introduction in the context of magnetic resonance can be found, for example, in [26]. The other circularly polarized component has only second-order effects, cf. Bloch–Siegert shift [26].

Frequently, the target specification is not given in terms of the required B_1 field but rather in terms of the required frequency of the Rabi oscillations [26] between the two spin states produced by the B_1 field, the so-called Rabi frequency. The Rabi frequency as a function of the B_1 field is given by [26]

$$\Omega_{\text{Rabi}} = \sqrt{2} \cdot B_1 \gamma \sin\theta \tag{3}$$

where γ is the gyromagnetic ratio, and θ represents the angle between the B_1 field vector and the NV center axis. Using (1)–(3), we can find the following closed-form expression for the required RF output power of the coil driver PA:

$$P_{\text{out}} = \frac{L_c \omega}{Q_c} \left(\frac{4\Omega_{\text{Rabi}}}{\sqrt{2}\mu_0 \gamma \sin\theta} \cdot \frac{\sqrt{(r^2 + z^2)^3}}{r^2} \right)^2. \tag{4}$$

According to (4), designing a coil with a high-quality factor and small radius reduces the required output power of the active device. However, a smaller coil radius comes at the expense of a reduced active coil volume and a larger roll-off along the z-axis perpendicular to the coil surface. For large Q-factor coils, the π-matching of Fig. 2(b) can lead to a small excitation bandwidth (BW), which restricts the BW of the NV magnetometer. Here, the BW can be extended by replacing the series capacitor C_s by a network of three capacitors according to Fig. 2(d). The corresponding simulation results for this wideband matching network are also included in Fig. 3(b), indicating the greatly increased BW and the moderate drop in coil current produced by this matching network.
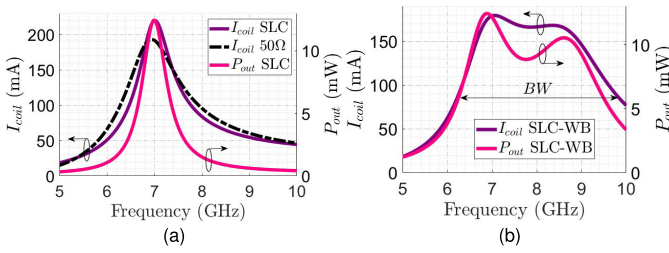
Fig. 3. Comparison of the OMNs shown in Fig. 2(b)–(d). Simulation parameters: $Z_{L,\text{opt}} = 86 + j67\ \Omega$, $Z_{\text{coil}} = 1.65 + j50\ \Omega$, and $f_{\text{sim}} = 7$ GHz. (a) Coil current and P_{out} versus frequency for series LC resonator (SLC) and 50-Ω match system. (b) Coil current and P_{out} versus frequency for the extended π-network for wideband designs (SLC-WB).

V. CIRCUIT IMPLEMENTATION

In this section, we present the details of the building blocks of the two ASICs that implement the MW electronics of the NV magnetometer architecture described in Section III and the custom-designed coil configuration.

A. 4-Channel Transmitter Chip

The architecture and the transistor-level schematics of the transmitter chip are shown in Figs. 4 and 5. According to Figs. 4 and 5, the TX driver chip consists of quadrature double-balanced active up-conversion mixers and a two-stage, 4-channel class-A PA. A double-balanced mixer topology has been selected due to its high isolation between the RF, LO, and IF ports. The RF and LO signals are routed using different RF metal layers to minimize residual coupling between these ports due to parasitic capacitances. A T-network of LCC components is used to match the output impedance of the mixer to the optimum source impedance of the PA's first stage over the desired frequency band. Thanks to the series C, the T-network also acts as a dc blocker. The first stage of the coil driver PA is implemented as a differential common-emitter (CE) amplifier (M_1-M_2) using high-speed heterojunction bipolar transistors (HS-HBTs) to maximize the power gain of this stage. The CE stage is biased using a current mirror configuration with an additional series base resistor to improve stability. However, this base resistor causes the actual breakdown voltage, V_{Br}, to be limited with a value between BV_{CEO} and BV_{CBO} due to injection efficiency reduction [27]. Fortunately, the reduced V_{Br} does not limit the maximum output power of the overall coil driver due to the moderate input level and voltage gain of the first PA stage. The output of the first stage is distributed to the four output power cells of the four-channel coil driver using differential transmission lines. The second-stage power cells are realized as hybrid cascode topologies featuring high-voltage device (HV-HBTs) as common-base (CB) devices (M_5 and M_6) and HS-HBTs as CE devices (M_3 and M_4) to maximize the output power and power gain [28] of each channel in the PA's second stage, respectively. The cascode configuration and the RC network at the base of its CE devices (M_3 and M_4) enhance the reverse isolation and reduce the unwanted low-frequency gain. Furthermore, by biasing the CB amplifier using a low-impedance source and a constant base–emitter voltage, V_{BE}, the actual breakdown voltage can

be pushed beyond BV_{CEO} [29], which increases the possible voltage swing and output power of the second stage. As shown in Fig. 4, the CE devices of the second stage are biased using the adaptive biasing circuit suggested in [30] that tracks the input power level and adjusts the dc current of the CE device, resulting in improved back-off efficiency and enhanced linearity. Here, a linearizing shunt capacitor, C_b, of $C_b = 3$ pF is chosen as a good compromise between die area and a low-ohmic RF path from node P_0 to gnd (see Fig. 4).

In this work, we decided to go with an off-chip coil for enhanced design flexibility. We implemented the matching on-chip mostly to avoid the large size of the off-chip components required to match all the four chip channels. More specifically, we have implemented a fully differential version of the extended π-network of Fig. 2(d), which provides an enhanced BW compared with the simple π-network of Fig. 2(b). The corresponding impedance trajectory and component values are shown in the Smith chart in Fig. 4 (left). The optimum load impedance of the selected active cascode device for different frequencies from 6 to 8 GHz is also shown in the Smith chart. Fig. 3 shows comparison of the simulated output power P_{out}, and the coil current swing of the simple π-match network of Fig. 2(b), a conventional 50-Ω-matching according to Fig. 2(c), and the implemented extended π-matching network of Fig. 2(d), for the actual implementation of the active cell (M_3–M_6). The simulations are performed for an input power level that corresponds to the maximum P_{out} of the active cell to evaluate the maximum possible value for I_{coil}. According to Fig. 3, the extended π-network greatly increases the achievable BW while suffering only from a moderate reduction in the maximum coil current swing from ≈ 200 to ≈ 150 mA.

B. Quadrature PLL Chip

The architecture of the presented QPLL together with transistor-level schematics of its most important building blocks is shown in Fig. 6. As an oscillator, the PLL uses a class-C VCO, similar to the one in [31], with a double-emitter–follower output buffer [see Fig. 6(c)]. The VCO core uses the largest HBT size of $40 \times 0.13\ \mu\text{m}^2$ in its cross-coupled pair to minimize the base resistance and, thereby, PN.

The width of the inductor trace ($w = 25\ \mu\text{m}$) was chosen as a compromise between coil quality factor, favoring a large trace width and the coil's SRF, favoring smaller trace width. The diode-based varactor was designed as an array of parallel varactors with a total size of $63 \times 0.3\ \mu\text{m}^2$ to achieve a tuning range of 26% around the center frequency of 14 GHz, ensuring a sufficient dynamic range of the NV-center-based sensor. More specifically, the length of the varactor unit cells corresponds to the minimum possible length to reduce the series resistance and, thereby, improve the VCO's PN, while the width and number of fingers are optimized to provide a suitable $C_{\text{max}}/C_{\text{min}}$ ratio and quality factor. Furthermore, the size of the VCO's tail current source was optimized to minimize flicker noise and avoid changes in the CM level of the VCO's differential output to avoid AM/PM conversion, which can deteriorate the VCO's PN, resulting in a final
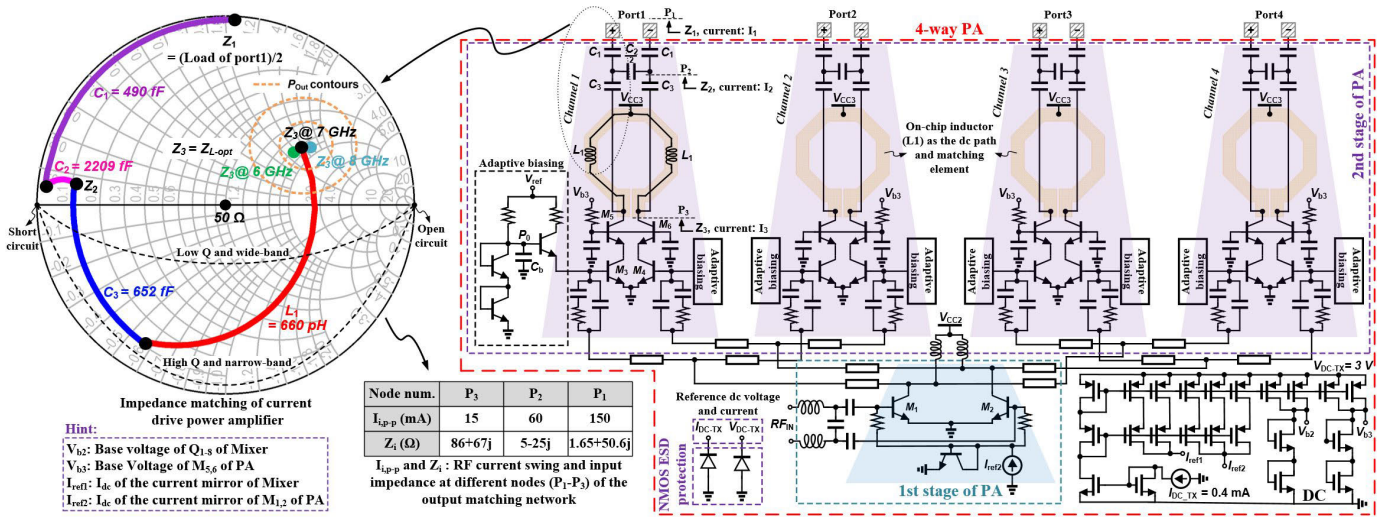
Fig. 4. Left: Illustration of the used output matching for maximum current delivery to the coil array. Right: Detailed schematics of the four-way PA.
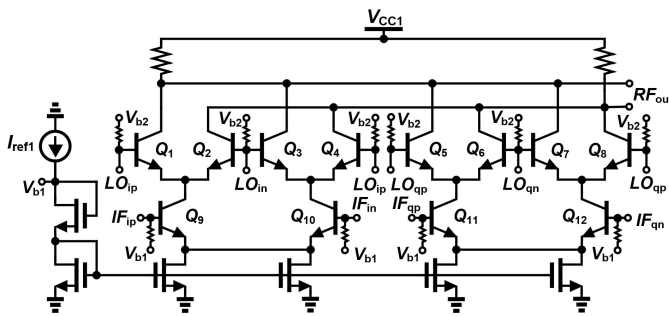

Fig. 5. Schematic of the IQ double-balanced up-conversion mixer.

size of the MOS tail current source of 40 μm/440 nm. In simulations (RC-extracted model of the active devices and an EM-extracted model of the passive elements and interconnection), the VCO achieves a tuning range of 26% and a PN of -118 dBc/Hz at 1-MHz offset from the carrier at 14 GHz. The divide-by-8 frequency divider following the VCO buffer has been implemented as a three-stage static ECL frequency divider based on a master–slave D flip-flop topology which also generates the required quadrature signals in the first divider stage [see Fig. 6(e)]. The bias current of the three divider stages has been scaled according to their respective operating frequencies from 12 mA for the first divider to 8 mA for the last divider stage. The quadrature outputs at half the VCO frequency are buffered using a differential CE amplifier [see Fig. 6(f)].

The phase detector (PD) of the PLL is implemented as a Gilbert cell mixer [see Fig. 6(b)] with a comparison frequency of 1.75 GHz and the target PLL BW of 35 MHz, which is needed to support advanced pulsed ODMR schemes. The PD is followed by an active loop filter (ALF) [see Fig. 6(d)], using HV-HBT devices to cover the required voltage tuning range of the VCO's varactor diodes. The PLL has a simulated (RC-extracted and EM-extracted models of the active and passive devices, respectively, and using an adjustable ALF supply voltage) tuning range of the quadrature LO output signal from 6.26 to 8.13 GHz.

C. Custom Coil on Glass Substrate

In [15], we have presented a custom-designed coil array consisting of four overlapping "phased" coils for the generation of the MW B_1 field. While this coil geometry is very suitable for the generation of homogeneous B_1 fields in the three narrow regions where two coils overlap, as it is, e.g., useful for quantum computing applications with spatially distributed qubits, it is not optimal for homogeneously exciting a large active region, e.g., for NV magnetometry, parallelized microscale NMR spectroscopy, or scanning NMR spectroscopy (see Section III). To provide a larger active coil volume with a higher B_1 field intensity, we conceived the coil design shown in Fig. 7(a). The basic idea of the presented coil is to take a conventional loop inductor and segment it such that—for a given overall outer coil diameter—each segment presents a lower inductance, facilitating its driving. To ensure that the resulting structure still produces a field mimicking that of a loop inductor, the individual segments are driven according to the scheme shown in Fig. 7(b). As presented in Section VI-B, we combine two of the four chip outputs to increase the current driving strength. The presented circular-shaped coil features an active area of $\pi \times 180 \times 180$ $(\mu\text{m})^2$. The coil is manufactured using a single 5-μm-thick copper layer on a glass substrate for optical transparency. As the substrate, we used a standard, 150-μm-thick microscope glass slide.

The coil was structured using maskless photolithography with a 5-nm Cr/200-nm Cu seed layer followed by electroplating to produce a final metal thickness of 5 μm. This relatively large thickness enhances the quality factor, which, according to the discussion in Section IV, results in a higher coil current swing. The coil geometry was optimized taking into account the optimum single-ended coil inductance of 2.3 nH/channel of the on-chip matching network of the TX chip and considering the mutual inductance of the two different coil segments as extracted from EM simulations and bondwire inductance, which is approximately 1 nH/mm. Here, to minimize the bondwire length, we leveled the TX chip and the coil surface
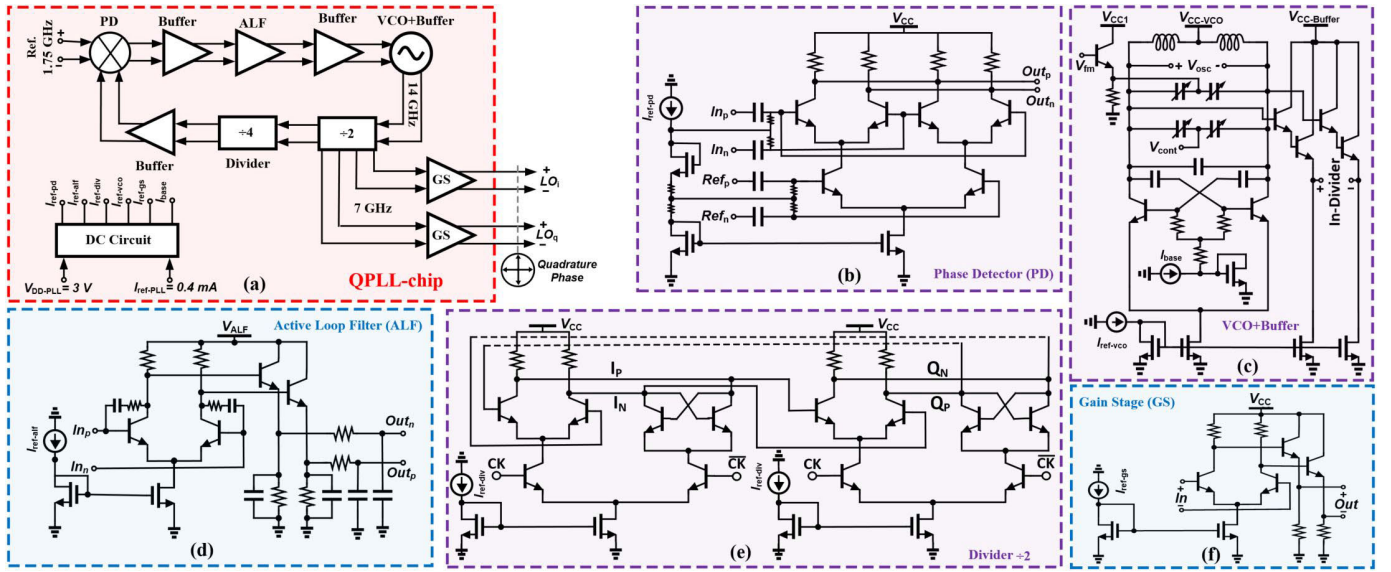
Fig. 6.   (a) Block diagram of the QPLL chip. (b)–(f) Simplified schematic of its main building blocks. (b) PD, (c) VCO, (d) ALF, (e) frequency divider, and (f) output gain stage.

by placing an additional microscope glass slide with a height of 150 μm underneath the coil substrate. The extraction of the electrical coil parameters and its geometry optimization were performed by EM simulations in Keysight PathWave ADS, while the homogeneity and intensity of the MW B_1 field were as evaluated by FEM simulations in COMSOL Multiphysics [see Fig. 7(b)]. Based on the EM model, the coil has a quality factor of $Q_c = 31$ at 7 GHz with an SRF of 47 GHz. Compared with the stripe array used in [11], assuming the same total RF current and a comparable size, the circular coil used in this article provides a higher B_1 amplitude up to a vertical distance from the coil/array surface that equals approximately the circular coil radius. Moreover, drilling a hole through the circular coil offers the possibility of inserting the diamond inside the coil, further improving B_1 homogeneity, and the overall form factor. Here, it should be noted that, in principle, stripe arrays can provide a better homogeneity both in the direction parallel and vertical to the array surface. In the presented design, which targets pulsed ODMR, we favored the higher B_1 over a further improvement in homogeneity since, for the given coil radius of 180 μm, the coil provides a homogeneity of better than 90% for distances from the surface up to 50 μm along the coil axis. Even at a distance of 100 μm from the coil surface, there is only a reduction of 33% in the MW magnetic field. In the coil plane, the presented coil provides a homogeneity of 92% across its entire diameter.

VI. EXPERIMENTAL RESULTS

A. Electrical Measurements

Prior to evaluating the presented NV magnetometer in its target application, we performed a series of electrical measurements to verify the functionality and benchmark the electrical performance of the chips presented in Sections V-A and V-B. The QPLL-chip and TX-chip, which were both fabricated in a 130-nm SiGe BiCMOS technology, occupy die areas of
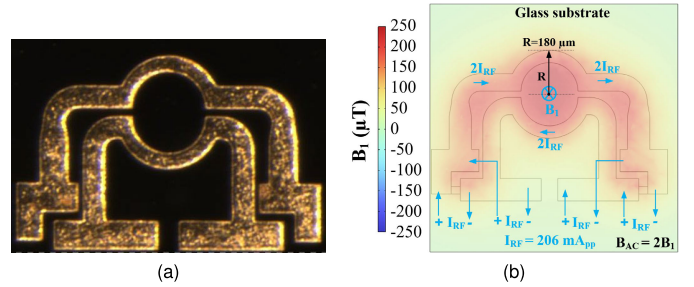

Fig. 7.   (a) Micrograph of the custom-designed coil on a glass substrate. (b) Distribution of the MW B_1 magnetic field over the coil ($z = 100$ μm) with a current swing of 206 mA$_{pp}$ (per ch) simulated in COMSOL.

1 and 1.04 mm^2, while consuming 130 and 380 mW from a 2.8-V supply voltage, respectively. Thanks to the adaptive biasing circuit, the dc power of the PA's second stage reduces to a few milliwatts during the OFF-state of the input RF pulse. A micrograph of the chips is presented in Section VI-B. By adjusting the ALF supply voltage (see Section V-B), the Ku-band QPLL achieves a measured tuning range from 12.8 to 16 GHz, corresponding to quadrature LO signals between 6.4 and 8 GHz [see Fig. 8(a)]. Next, we measured the PN and frequency noise performance of the QPLL chip at different carrier frequencies using a signal source analyzer (Rohde & Schwarz FSPN8). The corresponding PN spectra for different output frequencies are shown in Fig. 8(b). The PN at 1-MHz offset from the carrier frequency of 7 GHz is -122 dBc/Hz. Fig. 8(c) shows simulations of the total phase and the contribution of the individual building blocks of the PLL at a carrier frequency of 7 GHz and shows comparison of the simulated results against the measured total PN. The primary reason for the degraded noise performance at lower output frequencies is the gain reduction of the ALF due to the lower supply voltage, which effectively increases the noise contributions of the PD and the ALF to the total PN. The second reason for the increased PN is the lower quality factor of the varactor at lower RF frequencies. By sweeping the

TABLE I

PERFORMANCE SUMMARY AND COMPARISON AGAINST THE STATE-OF-THE-ART FOR THE QPLL CHIP

References	This work	TMTT' 20 [32]	IEEE A.' 20 [33]	TMTT' 17 [34]	JSSC' 14 [35]	JSSC' 13 [36]
Freq. (GHz) (FTR)	12.8 – 16 (22%)	20.52 – 24.88 (19%)	5.4 – 8 (38.8%)	29.5 – 33.4 (12.4%)	4.8 – 6.9 (34%)	15.6 – 17.1 (9.17%)
PLL's BW (MHz)	35	N.A.	N.A.	N.A.	N.A.	N.A.
Phase Noise @ 10 kHz (dBc/Hz)	-103 @ 7 GHz	-90.17 @ 10.5 GHz	-79 @ 6.86 GHz	-80 @ 30.24	-86.45 @ 6.56 GHz	-69 @ 16.45
Phase Noise @ 1 MHz (dBc/Hz)	-122 @ 7 GHz	-118.21 @ 10.5 GHz	-101.4 @ 6.86 GHz	-97 @ 30.24	-114 @ 6.56 GHz	-115.3 @ 16.45
Spur (dBc)	-71	-70	N.A.	-40	N.A.	N.A.
P_{out} (dBm)	-8 ∼ -1	∼ -5	∼ -8.89	-12 ∼ -5	∼ -14.89	N.A.
FoM^a @10kHz (dBc/Hz)	198.5	188.83	181.25	191.62	N.A	170.58
FoM$_T$^{b} @1MHz (dBc/Hz)	184.35	182.45	175.43	170.49	N.A.	176.13
Ref. Freq. (MHz)	1750	155.52	210 ∼ 112	120	80	50
P_{diss} (mW)	138	150	28	63	326/333 (Rx/Tx)	188
Area (mm^2)	1	1.232	1.92	5.2	1^c	N.A.
Technology	130 nm BiCMOS	120 nm BiCMOS	65 nm CMOS	180 nm BiCMOS	130 nm BiCMOS	250 nm BiCMOS

a: $FoM = -\mathcal{L}(f_{off}) + 20\log\left(\frac{f_0}{f_{off}}\right) - 10\log\left(\frac{P_{DC}}{1mW}\right)$; b: $FoM_T = FoM + 20\log\left(\frac{TR\%}{10(\%)}\right)$; c: estimated from the total size (total TR: 8.75 mm^2).

supply voltage of the frequency divider and gain stage, the QPLL chip can drive the TX chip with a tunable input power at its LO port from −8 to −1 dBm [see Fig. 8(d)]. The measured small-signal PLL BW is 35 MHz [see Fig. 8(e)]. A measured output spectrum of the PLL chip for an output frequency of 7 GHz is shown in Fig. 8(f). The measured SFDR in the spectral range from 5 to 9 GHz is approximately 71 dB. The measured static imbalance between the I and Q signals at 7 GHz is equal to 0.8°. Table I summarizes the performances of the proposed QPLL chip and shows comparison against the current state-of-the-art in frequency synthesizers in a similar frequency range. According to Table I, the presented PLL achieves a state-of-the-art figure-of-merit (FoM) both at 10-kHz and 1-MHz offset from the carrier.

B. ODMR Magnetometry Measurements

All the ODMR measurements were conducted using the coil structure presented in Section V-C. The micrograph of the proposed setup for quantum magnetometry using the two ASICs for MW generation and the coil on a glass substrate is shown in Fig. 9(a). As diamond, we used a prototype sample from Element Six with a natural abundance of ^{13}C and a 10-μm chemical vapor deposition (CVD)-grown layer of NV centers with a concentration of 2.5 ppm.[1] This diamond is positioned atop the coil such that the NV layer is facing the coil and, thereby, experiences the maximum MW B_1 field. For all the experiments, one of the four NV center axes was aligned parallel to the B_0 field such that the measured frequency shift is directly proportional to the full magnitude of the B_0 field.

The setup of Fig. 9(b), including the diamond, is placed inside an electromagnet to generate the required static magnetic field of $B_0 = 146$ mT. According to Section II, this dc magnetic field induces a Zeeman splitting of the energy levels of the NV centers inside the diamond with resonance frequencies at $f_{MW} = 2.87$ GHz $\pm (\gamma/2\pi)B_0$. For the used
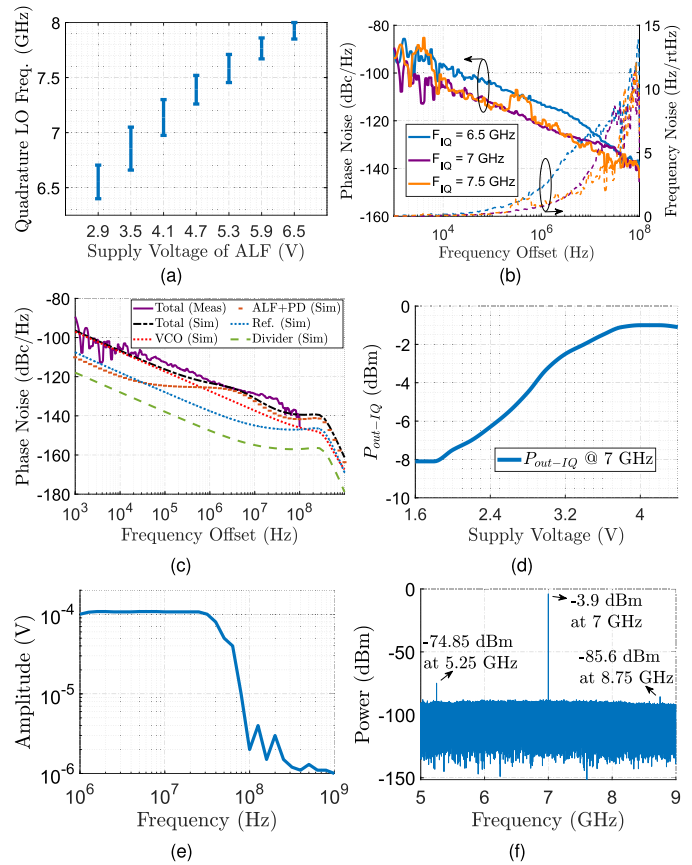

Fig. 8. Measured results of the QPLL chip. (a) Locking range at different supply voltages of the ALF. (b) PN and frequency noise of the IQ outputs at different frequencies versus frequency offset from the carrier. (c) Measured and simulated PN at a center frequency of 7 GHz, including the simulated contributions of the individual PLL building blocks. (d) Output power of the IQ signal versus supply voltage of the output gain stage of the QPLL chip. (e) Measured PLL small signal BW. (f) Measured PLL output spectrum at an output frequency of 7 GHz.

---

[1] Further information on the diamond can be obtained from the authors upon request.

B_0 field around 150 mT, the resonance frequencies occur at around 7 GHz, the operating frequency of the presented
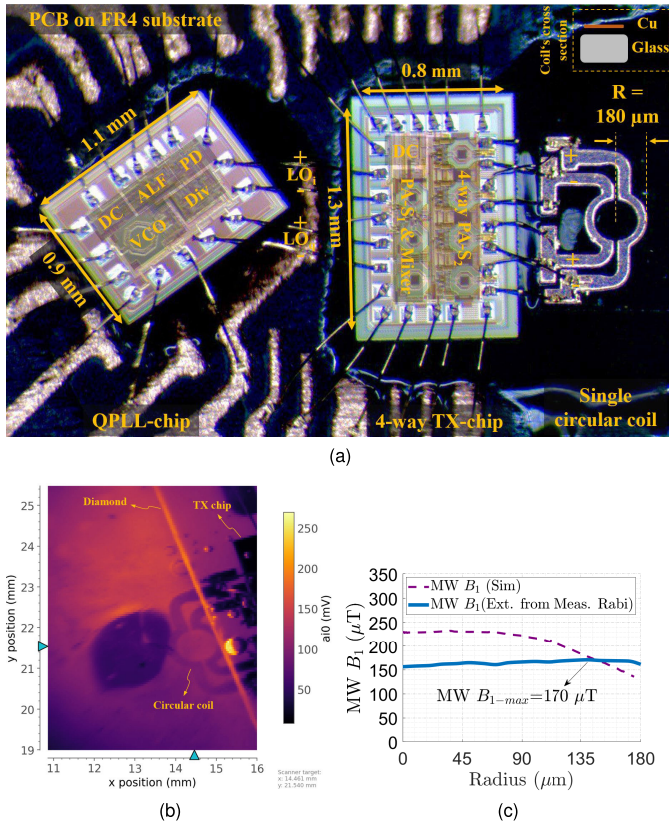
Fig. 9. (a) Micrograph of the probe head containing from left to right: the QPLL chip, the four-way TX chip, and custom excitation coil on glass substrate. (b) Micrograph of the excitation coil loaded with a diamond sample. (c) Simulated and measured homogeneity of the MW B_1 field. The measured B_1 field has been extracted from measured Rabi oscillations at different positions across the diamond.
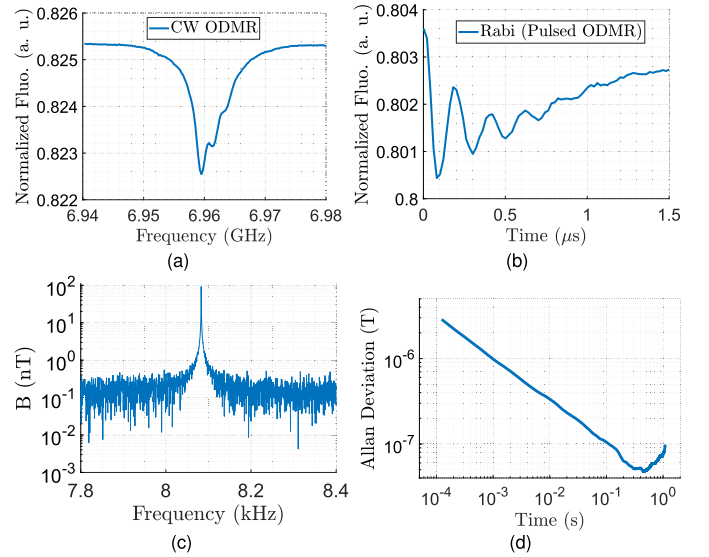

Fig. 10. (a) Measured CW ODMR spectrum at a magnetic field of about 150 mT. (b) Measured Rabi oscillations in a pulsed ODMR experiment. (c) Measured spectra of an external test magnetic field to measure the LOD. (d) Measured Allan deviation of the presented sensor.
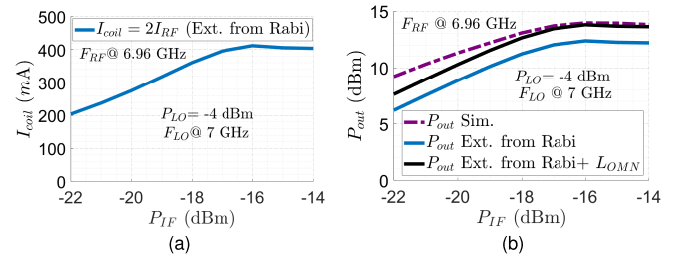

Fig. 11. (a) Coil current extracted from Rabi oscillation measurements. (b) Comparison of the RF output power of each channel [chi ($i = 1$–4)] of the TX chip extracted from Rabi oscillation measurements (with and without the matching network loss ($L_{OMN} = 1.42$ dB) at 6.96 GHz) against simulations.

ASICs. For all the experiments, we used a green laser (Coherent Verdi G2) for NV center initialization and readout with a wavelength of 532 nm and a circular spot size with a diameter of approximately 20 μm [full width at half maximum (FWHM)] with an rms noise performance of better than 0.03% over a BW of 10 Hz–100 MHz. The resulting optical power in the illuminated part of the NV center layer was approximately 150 mW. A piezoelectric translation stage is used to precisely position the green laser light with respect to the diamond surface.

To detect the fluorescence light emitted by the diamond, we used a commercial photodiode (Hamamatsu, S1337-66BR). The photodiode signal is amplified using a commercial transimpedance amplifier (TIA) (FEMTO DHPCA-100), with a gain of 10^5 V/A. The TIA output signal is digitized using an ADC card with a 200-MHz BW and 16-bit resolution. The green laser light is deflected with a dichroic mirror before being directed and focused on the NV centers and the emitted fluorescence is additionally filtered through a 650-nm longpass filter before reaching the photodiode. Our setup provides an estimated attenuation by a factor larger than 10^5 in the range of 200–641 nm. With the laser setup described above, we illuminated and measured approximately 10^9 NV centers, with a fluorescence level of about 20 μW.

Enabled by the wide BW of the presented system, we performed the CW measurements in the so-called frequency-sweep mode (see Section II). To do so, we swept the IF signal from 0 to 100 MHz while keeping the LO signal generated by the QPLL at a fixed frequency of 7 GHz, resulting in MW excitation signals between 6.9 and 7 GHz at the output of the 4-channel TX chip. The corresponding CW ODMR spectrum is shown in Fig. 10(a). The spectrum shows the expected dip in the fluorescence signal induced by the resonant MW B_1 field at a frequency of 6.96 GHz. After the CW ODMR measurement, we performed a pulsed ODMR experiment, in which we swept the length of an on-resonance, i.e., with a frequency of $f_{MW} = 6.96$ GHz, excitation pulse to monitor the Rabi oscillations of the spin ensemble. The measured Rabi oscillations are shown in Fig. 10(b). From the Rabi oscillation frequency, we extracted the MW B_1 field magnitude using (3) and the angle $\theta = 54.7°$ between the B_1 field vector and the NV center axis parallel to the B_0 field. More specifically, from the maximum measured Rabi frequency of 5.49 MHz we extracted a maximum B_1 field of 170 μT. From this extracted B_1 field value, we calculated a maximum coil current of 412 mA$_{pp}$ (i.e., 206 mA$_{pp}$/ch) at 7 GHz. Next, we measured the Rabi oscillation across the coil's radius to evaluate the homogeneity of the single circular coil. To this

TABLE II

COMPARISON WITH THE STATE-OF-THE-ART IN MINIATURIZED NV MAGNETOMETERS INCORPORATING CUSTOM ASICs

References	This work	Nature Elec.' 19 [10]	JSSC' 21 [11]	Tran. Ins. Meas.' 22 [12]
Freq. (GHz)	$6.4 - 8$	$2.6 - 3.1$	Around 2.87^a	$2.67 - 3.12$ & $2.58 - 3.21$
Phase Noise (dBc/Hz)	-102 @ 7 GHz, Δf^b: 3 kHz -116 @ 7 GHz, Δf : 100 kHz	-90 @ 2.87 GHz Δf: 1.5 kHz	-88 @ 2.87 GHz Δf: 3 kHz	-91 @ 2.87 GHz, Δf: 100 kHz -105 @ 2.87 GHz, Δf: 100 kHz
Integrated building blocks	B_1 generation	B_1 generation Optical detection	B_1 generation Optical detection	B_1 generation Optical detection
Rabi Freq. (MHz)	3.66^c - 5.49^d	N.A.	1.2	N.A.
Active Area (μm^2)	$(88.84 \times 10^4)^c$ $(10.17 \times 10^4)^d$	0.25×10^4	2.4×10^4	N.A.
LOD (nT/$\sqrt{Hz}$)	AC: 0.3 DC: 32	DC: 3.21×10^4	DC: 245	DC: 1.07×10^5 DC: 8.52×10^3
Technology	130 nm BiCMOS	65 nm CMOS	65 nm CMOS	HMICs GaAs

a: The frequency range was not specified; b: Δf = frequency offset; c: using the 4-coil array [15]; d: using the single circular coil.

end, we moved the xyz translation stage and monitored the pulsed ODMR signal. The extracted homogeneity of the MW magnetic field is shown in Fig. 9(c). According to Fig. 9(c), the presented coil achieves approximately 91% homogeneity in the B_1 field across the coil diameter. Furthermore, we measured the Rabi oscillation versus IF input power at 40 MHz. The extracted coil current swing from the Rabi oscillations is depicted in Fig. 11(a). From these Rabi oscillations and the theory presented in Section IV, we calculated the RF output power P_{out} and compared it against extracted level simulations. The corresponding results are shown in Fig. 11(b), displaying a good agreement between simulations and measurements, when taking the loss of the OMN into account, thereby validating the theoretical model of Section IV. Finally, to determine the performance of the proposed system in its target application of precision magnetometry, we also measured the ac and dc magnetic field limits of detection (LODs). Here, we first measured the ac sensitivity using the Qdyne protocol [18]. To this end, we applied an external test ac magnetic field with a frequency of 994 kHz using an auxiliary loop coil beneath the MW coil's substrate. From the magnetic field of 92 nT produced by the auxiliary coil and the measured signal-to-noise ratio (SNR) of 333, we extracted an ac field sensitivity of 300 pT/$\sqrt{Hz}$ [see Fig. 10(c)]. Next, we measured the Allan deviation [37] of the presented sensor to assess the sources of noise and instability in our ODMR setup and determine the optimal integration time for minimum integrated noise. As shown in Fig. 10(d), the Allan deviation reaches its minimum value of 47.6 nT for an averaging time of $T_{av} \approx 460$ ms, corresponding to a dc LOD of 32 nT/$\sqrt{Hz}$. The observed plateau in the Allan deviation arises from fluctuations in the external magnetic field, preventing improvements in the dc accuracy beyond averaging times of 460 ms. The limited B_0 field stability of the used electromagnet in part explains the difference between the measured ac and dc LODs. The performance of the presented quantum magnetometry system is compared against the current state-of-the-art in NV center magnetometers using custom ASICs in Table II, highlighting the excellent performance of the presented system. Here, our system achieves the best LOD but with a lower integration level compared with the designs in [10] and [11], which also feature an on-chip optical detection of the ODMR signal.

In contrast to prior art, the presented design was also tested for ac magnetometry, displaying an excellent, sub-nT ac LOD.

VII. CONCLUSION

In this article, which is an extended version of [15], we have presented an NV center-based magnetometer that uses two ASICs for the generation and amplification of the required MW signals. The MW frontend of the transmitter ASIC, including the newly proposed matching network, has been co-designed with an off-chip coil to maximize the coil current and, thereby, the MW magnetic field B_1 produced by the system. Together with two matching networks that are suitable for maximizing the coil current in an energy-efficient manner, we presented closed-form expressions that allow the designer to calculate the required output MW power of the active device for a certain required MW magnetic field B_1 or Rabi oscillation. The closed-form expressions are validated both by simulations and measurements using the presented prototype implementation. The presented QPLL chip, which generates the quadrature LO signals for the 4-channel TX chip, displays an improved FoM compared with prior arts. The excellent performance of the presented ODMR system has been validated both in CW and pulsed ODMR experiments. Compared with conventional state-of-the-art NV magnetometers, the presented implementation significantly reduces the size, cost, and power consumption of the sensor electronics. The presented system achieves excellent dc magnetic field LOD and provides a very good ac sensitivity of 300 pT/Hz$^{1/2}$ as a promising candidate for future chip-integrated spin control platforms for NV centers. In the future, we will extend the presented MW electronics platform by a low-noise current readout for the ODMR photocurrent to reduce the footprint and power consumption of the overall magnetometer further.

REFERENCES

[1] J. S. Hodges, N. Y. Yao, D. Maclaurin, C. Rastogi, M. D. Lukin, and D. Englund, "Timekeeping with electron spin states in diamond," *Phys. Rev. A, Gen. Phys.*, vol. 87, no. 3, Mar. 2013, Art. no. 032118.

[2] J. F. Barry et al., "Optical magnetic detection of single-neuron action potentials using quantum defects in diamond," *Proc. Nat. Acad. Sci. USA*, vol. 113, no. 49, pp. 14133–14138, Nov. 2016.

[3] A. Kuwahata et al., "Magnetometer with nitrogen-vacancy center in a bulk diamond for detecting magnetic nanoparticles in biomedical applications," *Sci. Rep.*, vol. 10, no. 1, p. 2483, Feb. 2020.

[4] M. H. Abobeih et al., "Atomic-scale imaging of a 27-nuclear-spin cluster using a quantum sensor," *Nature*, vol. 576, no. 7787, pp. 411–415, Dec. 2019.

[5] G. Kucsko et al., "Nanometre-scale thermometry in a living cell," *Nature*, vol. 500, no. 7460, pp. 54–58, Jul. 2013.

[6] H. J. Mamin et al., "Nanoscale nuclear magnetic resonance with a nitrogen-vacancy spin sensor," *Science*, vol. 339, no. 6119, pp. 557–560, Feb. 2013.

[7] A. Horsley et al., "Microwave device characterization using a widefield diamond microscope," *Phys. Rev. Appl.*, vol. 10, no. 4, Oct. 2018, Art. no. 044039.

[8] J. R. Maze et al., "Nanoscale magnetic sensing with an individual electronic spin in diamond," *Nature*, vol. 455, no. 7213, pp. 644–647, Oct. 2008.

[9] G. Balasubramanian et al., "Ultralong spin coherence time in isotopically engineered diamond," *Nature Mater.*, vol. 8, no. 5, pp. 383–387, May 2009.

[10] D. Kim, M. I. Ibrahim, C. Foy, M. E. Trusheim, R. Han, and D. R. Englund, "A CMOS-integrated quantum sensor based on nitrogen–vacancy centres," *Nature Electron.*, vol. 2, no. 7, pp. 284–289, Jul. 2019.

[11] M. I. Ibrahim, C. Foy, D. R. Englund, and R. Han, "High-scalability CMOS quantum magnetometer with spin-state excitation and detection of diamond color centers," *IEEE J. Solid-State Circuits*, vol. 56, no. 3, pp. 1001–1014, Mar. 2021.

[12] Y. Gao et al., "Diamond NV centers based quantum sensor using a VCO integrated with filtering antenna," *IEEE Trans. Instrum. Meas.*, vol. 71, pp. 1–12, 2022.

[13] K. Khan et al., "A 12.2 to 14.9 GHz injection-locked VCO array with an on-chip 50 MHz BW semi-digital PLL for transient spin manipulation and detection," in *Proc. IEEE 65th Int. Midwest Symp. Circuits Syst. (MWSCAS)*, Aug. 2022, pp. 1–4.

[14] M. A. Hassan et al., "Towards single-cell pulsed EPR using VCO-based EPR-on-a-chip detectors," *Frequenz*, vol. 76, nos. 11–12, pp. 699–717, Mar. 2023.

[15] H. Lotfi et al., "A diamond quantum magnetometer based on a chip-integrated 4-way transmitter in 130-nm SiGe BiCMOS," in *Proc. IEEE Radio Freq. Integr. Circuits Symp. (RFIC)*, Jun. 2023, pp. 253–256.

[16] M. W. Doherty, N. B. Manson, P. Delaney, F. Jelezko, J. Wrachtrup, and L. C. L. Hollenberg, "The nitrogen-vacancy colour centre in diamond," *Phys. Rep.*, vol. 528, no. 1, pp. 1–45, Jul. 2013.

[17] F. A. Hahl et al., "Magnetic-field-dependent stimulated emission from nitrogen-vacancy centers in diamond," *Sci. Adv.*, vol. 8, no. 22, Jun. 2022, Art. no. eabn7192.

[18] S. Schmitt et al., "Submillihertz magnetic spectroscopy performed with a nanoscale quantum sensor," *Science*, vol. 356, no. 6340, pp. 832–837, May 2017.

[19] R. D. Allert, K. D. Briegel, and D. B. Bucher, "Advances in nano- and microscale NMR spectroscopy using diamond quantum sensors," *Chem. Commun.*, vol. 58, no. 59, pp. 8165–8181, 2022.

[20] J. Keeler, *Understanding NMR Spectroscopy*. Chichester, U.K.: Wiley, 2005.

[21] V. Stepanov, F. H. Cho, C. Abeywardana, and S. Takahashi, "High-frequency and high-field optically detected magnetic resonance of nitrogen-vacancy centers in diamond," *Appl. Phys. Lett.*, vol. 106, no. 6, Feb. 2015, Art. no. 063111.

[22] S. C. Cripps, *RF Power Amplifiers for Wireless Communications*, 2nd ed. Norwood, MA, USA: Artech House, 2006.

[23] S. C. Cripps, "A theory for the prediction of GaAs FET load-pull power contours," in *IEEE MTT-S Int. Microw. Symp. Dig.*, May 1983, pp. 221–223.

[24] X. Yang and A. Babakhani, "A single-chip electron paramagnetic resonance transceiver in 0.13-μ m SiGe BiCMOS," *IEEE Trans. Microw. Theory Techn.*, vol. 63, no. 11, pp. 3727–3735, Nov. 2015.

[25] H. Lotfi, M. A. Hassan, M. Kern, and J. Anders, "A compact C-band EPR-on-a-chip transceiver in 130-nm SiGe BiCMOS," in *Proc. 17th Conf. Ph.D Res. Microelectron. Electron. (PRIME)*, Jun. 2022, pp. 157–160.

[26] A. Schweiger and G. Jeschke, *Principles of Pulse Electron Paramagnetic Resonance*. London, U.K.: Oxford Univ. Press, 2001.

[27] C. M. Grens, "A comprehensive study of safe-operating-area, biasing constraints, and breakdown in advanced SiGe HBTs," M.S. thesis, School Elect. Comput. Eng., Georgia Inst. Technol., Atlanta, GA, USA, 2005.

[28] I. Petricli, H. Lotfi, and A. Mazzanti, "Analysis and design of D-band cascode SiGe BiCMOS amplifiers with gain-bandwidth product enhanced by load reflection," *IEEE Trans. Microw. Theory Techn.*, vol. 69, no. 9, pp. 4059–4068, Sep. 2021.

[29] C. M. Grens, J. D. Cressler, and A. J. Joseph, "Large-signal performance, linearity, and reliability characteristics of aggressively-biased cascode SiGe HBTs for power amplifier applications," in *Proc. IEEE Bipolar/BiCMOS Circuits Technol. Meeting*, Sep. 2007, pp. 135–138.

[30] Y. S. Noh and C. S. Park, "PCS/W-CDMA dual-band MMIC power amplifier with a newly proposed linearizing bias circuit," *IEEE J. Solid-State Circuits*, vol. 2, no. 9, pp. 1096–1099, Sep. 2002.

[31] A. Mazzanti and P. Andreani, "A push–pull class-C CMOS VCO," *IEEE J. Solid-State Circuits*, vol. 48, no. 3, pp. 724–732, Mar. 2013.

[32] E. Wagner, O. Shana'a, and G. M. Rebeiz, "A very low phase-noise transformer-coupled oscillator and PLL for 5G communications in 0.12 μ m SiGe BiCMOS," *IEEE Trans. Microw. Theory Techn.*, vol. 68, no. 4, pp. 1529–1541, Apr. 2020.

[33] S. Ma, T. Wu, and J. Ren, "A quadrature PLL with phase mismatch calibration for 32GS/s time-interleaved ADC," *IEEE Access*, vol. 8, pp. 219695–219708, 2020.

[34] N. Mahalingam, Y. Wang, B. K. Thangarasu, K. Ma, and K. S. Yeo, "A 30-GHz power-efficient PLL frequency synthesizer for 60-GHz applications," *IEEE Trans. Microw. Theory Techn.*, vol. 65, no. 11, pp. 4165–4175, Nov. 2017.

[35] J. Yu et al., "An X-band radar transceiver MMIC with bandwidth reduction in 0.13 μ m SiGe technology," *IEEE J. Solid-State Circuits*, vol. 49, no. 9, pp. 1905–1915, Sep. 2014.

[36] G. W. de Jong, D. M. W. Leenaerts, and E. van der Heijden, "A fully integrated Ka-band VSAT down-converter," *IEEE J. Solid-State Circuits*, vol. 48, no. 7, pp. 1651–1658, Jul. 2013.

[37] A. A. Wood, A. Stacey, and A. M. Martin, "DC quantum magnetometry below the Ramsey limit," *Phys. Rev. Appl.*, vol. 18, no. 5, Nov. 2022, Art. no. 054019.

Hadi Lotfi (Graduate Student Member, IEEE) received the M.Sc. degree in electrical engineering from the Sharif University of Technology, Tehran, Iran, in 2015, focusing on radio frequency circuit design. He is currently pursuing the Ph.D. degree in electrical engineering with the University of Stuttgart, Stuttgart, Germany.

From 2017 to 2018, he was a Researcher with the Analog Integrated Circuit (AIC) Laboratory, University of Pavia, Pavia, Italy, where he was involved in IC design for high-speed communications and millimeter-wave systems. His research interests include RF and microwave integrated circuits design for applications such as wireless communication systems, biomedical, and quantum sensing.

Mr. Lotfi was a recipient of the Ph.D. Research in Microelectronics and Electronics (PRIME) Conference Gold Leaf Certificate in 2022.
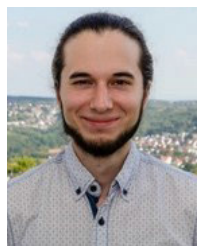
Michal Kern received the master's degree in physical engineering and nanotechnologies from the Brno University of Technology, Brno, Czech Republic, in 2015, and the Ph.D. degree from the Institute of Physical Chemistry, University of Stuttgart, Stuttgart, Germany, in 2021.

From 2020 to 2023, he held a post-doctoral position with the Institute of Smart Sensors, University of Stuttgart, where he has been a Lecturer and a Research Group Leader since 2023. His current research interests include integrated circuits for magnetic resonance, quantum sensing, and spin information processing applications.

Dr. Kern was a recipient of the 2020/2021 International EPR Society Best Paper Award.

Qing Yang, photograph and biography not available at the time of publication.

Thomas Unden received the master's degree in physics from the Institute for Quantum Optics, University of Ulm, Ulm, Germany, in 2014.

From 2014 to 2018, he was a Doctoral Researcher at the Fedor Jelezko's Laboratory, University of Ulm, focusing on quantum information processing with color centers in diamond. Since 2019, has been with NVision Imaging Technologies GmbH, Ulm, where his research has centered on demonstrating high-resolution NMR of ultrasmall quantities in the picoliter regime. One promising application is the detection and study of the metabolism of a single cell.

Nico Striegler is currently pursuing the master's degree with the Physics Department, University of Ulm, Ulm, Germany. He is currently working on his master's thesis project devoted to the development of ultrasensitive nuclear magnetic resonance at the Institute of Quantum Optics, University of Ulm, in collaboration with NVision Imaging Technologies GmbH, Ulm.

Jochen Scharpf, photograph and biography not available at the time of publication.

Patrick Schalberger studied electrical engineering at the University of Stuttgart, Stuttgart, Germany. He received the Diploma degree in 2005 and the Ph.D. degree in 2012.

Since then, he has led or administrated several research projects covering various aspects of large area microelectronic manufacturing. His current research interests include development of advanced driving circuits for system-on-panel (SOP) displays and surface MEMS applications.

Rainer Stöhr received the master's degree in physics from the University of Oregon, Eugene, OR, USA, in 2005, the Dipl.-Phys. degree from the University of Stuttgart, Stuttgart, Germany, in 2007, and the Ph.D. degree in physics from the 3rd Institute of Physics, University of Stuttgart, in 2012, focusing on non-linear optics in graphene.

From 2014 to 2016, he held a joint post-doctoral position at Harvard University, Cambridge, MA, USA, and the University of Waterloo, Waterloo, ON, Canada, working on scanning probe magnetometry with NV centers in diamond. Since 2016, he has been a Senior Lecturer and a Research Group Leader with the Center for Applied Quantum Technologies, University of Stuttgart, working on quantum sensing applications with NV centers and nanofabrication of quantum materials.

Ilai Schwartz received the Ph.D. degree (summa cum laude) in physics from the University of Ulm, Ulm, Germany.

He is currently a Co-Founder and the Chief Technology Officer at NVision Imaging Technologies GmbH, Ulm, bringing diverse backgrounds in research and development (R&D) management, deep quantum physics, and management consulting. He has over 15 years of experience leading technological R&D projects and product development, including cyber security start-ups, and as a coordinator of large-scale quantum physics projects. He is also a McKinsey & Company Alumni, having gained valuable experience in corporate strategy and PharmaCo operations. He is an inventor of more than ten breakthrough patents in quantum hyperpolarization and led the NVision Development Team in achieving the first viable, room-temperature polarizer for metabolic MRI. He is the coordinator of several high-profile quantum technologies projects.

Philipp Neumann, photograph and biography not available at the time of publication.

Jens Anders (Senior Member, IEEE) received the master's degree from the University of Michigan, Ann Arbor, MI, USA, in 2005, the Dipl.-Ing. degree from Leibniz University Hannover, Hannover, Germany, in 2007, and the Ph.D. degree from the École Polytechnique Fédérale de Lausanne, Lausanne, Switzerland, in 2011.

From 2013 to 2017, he was an Assistant Professor of biomedical integrated sensors with the Institute of Microelectronics, University of Ulm, Ulm, Germany. He is currently a Full Professor and the Director of the Institute of Smart Sensors, University of Stuttgart, Stuttgart, Germany. Since 2022, he has also been the Director of the Institute for Microelectronics Stuttgart (IMS CHIPS), Stuttgart. He has authored or coauthored several books and book chapters as well as more than 150 journal articles and conference papers. His current research interests include circuit design for sensing applications, including materials science as well as biomedical and quantum sensing.

Dr. Anders served as a Program Committee Member for various conferences, including International Solid-State Circuits Conference (ISSCC), European Solid-State Circuits Conference (ESSCIRC), European Solid-State Device Research Conference (ESSDERC), and IEEE Sensors. He received the 2003 President's Award of the Leibniz University of Hannover, the 2006 Best Thesis Award of the VDE Chapter Hannover, the E.ON Future Award 2007, the VDE ITG ISS Study Award 2008, the ICBME 2008 Outstanding Paper Award, the VDE ITG Outstanding Publication Award 2012, the IEEE Sensors 2017 Best Live Demo Award, the 2019 Helmholtz Center for Energy and Materials Berlin Technology Transfer Award, and one of the Sony Europe Research Awards 2021. He has been an Associate Editor of the IEEE TRANSACTIONS ON CIRCUITS AND SYSTEMS II (TCASII) and a Guest Editor of the IEEE JOURNAL OF SOLID-STATE CIRCUITS (JSSC) and IEEE SOLID-STATE CIRCUITS LETTERS (SSC-L).